



HAL
open science

**Physical, chemical and thermomechanical
characterisation of glass textile-reinforced concretes
(TRC): Effect of elevated temperature and of
cementitious matrix nature on properties of TRC**

Tala Tlajji, Xuan Hong Vu, Marie Michel, Emmanuel Ferrier, Amir Si Larbi

► **To cite this version:**

Tala Tlajji, Xuan Hong Vu, Marie Michel, Emmanuel Ferrier, Amir Si Larbi. Physical, chemical and thermomechanical characterisation of glass textile-reinforced concretes (TRC): Effect of elevated temperature and of cementitious matrix nature on properties of TRC. *Materials Today Communications*, 2020, 25, pp.101580 -. 10.1016/j.mtcomm.2020.101580 . hal-03492212

HAL Id: hal-03492212

<https://hal.science/hal-03492212>

Submitted on 30 Aug 2022

HAL is a multi-disciplinary open access archive for the deposit and dissemination of scientific research documents, whether they are published or not. The documents may come from teaching and research institutions in France or abroad, or from public or private research centers.

L'archive ouverte pluridisciplinaire **HAL**, est destinée au dépôt et à la diffusion de documents scientifiques de niveau recherche, publiés ou non, émanant des établissements d'enseignement et de recherche français ou étrangers, des laboratoires publics ou privés.



Distributed under a Creative Commons Attribution - NonCommercial 4.0 International License

25 ultimate stress and the post-cracked composite stiffness of TRC corresponds to dehydration of
26 components of cementitious matrix. However, between 110 °C and 300 °C, with water
27 molecules released, hydration of anhydrous particles of the cementitious matrix (mortar) occurs,
28 a gain in the ultimate stress and the cracked-composite stiffness of glass TRC consequently
29 occurs.

30 KEYWORDS: Textile-reinforced concrete (TRC); elevated temperature; thermomechanical
31 characterisation; physical and chemical characterisation; thermal characterisation (TMA, TGA,
32 DSC); XRD and FTIR analyses; tomography observation

33 1 INTRODUCTION

34 Development of composite materials in civil engineering involves two main steps: design and
35 construction of structures or parts of composite structures, reinforcement and repair of existing
36 structures [1,2,3,4]. The last family of rigid composite materials comprise fibre/cement
37 composites, in which the polymer matrices are replaced by mineral matrices such as hydraulic
38 binders, phosphate binders, sulphate binders, and magnesium binders.

39 The tensile, bending or shear behaviours of textile-reinforced concretes at ambient temperature
40 have been experimentally investigated [5,6,7,8]. Until now, there were some fire tests
41 performed on glass or carbon TRC specimens [9], TRC thin-plates with different cementitious
42 materials [10], on high-performance concrete thin-plates, reinforced with basalt fibre-reinforced
43 polymer mesh [11], on carbon fibre-reinforced, fine-grained concrete [12], and on I-shaped
44 beams, reinforced with glass-fibre and carbon-fibre mesh grids [13,14]. These studies
45 highlighted that when TRC was subjected to elevated temperatures or fire, thermal and
46 mechanical properties of TRC significantly changed with increasing temperature.

47 Thermal characterisation of the cementitious matrix is necessary to quantify its expected
48 structural performance and integrity under high temperatures. It has been shown that the
49 mechanical behaviour of cement is related to its porosity and phase changes [15,16]. Some
50 studies have focused on thermal behaviour of mortars (or concretes) containing different

51 discontinuous fibres under thermal exposure using cone calorimeter heating [17,18],
52 thermogravimetry (TG) and differential scanning calorimetry (DSC) [19,20,21]. Few studies
53 focused on microstructure evolution and decomposition of cement composite under high
54 temperature [22,23,24]. Physical, mechanical and experimental investigations mentioned above
55 [20,25] allowed identifying effect of parameters related to composition of the cementitious
56 matrix (as porosity, different discontinuous fibres) on thermal properties and microstructure of
57 hardened cementitious mortars.

58 Until now, because of a lot of experimental difficulties, there were little studies focusing on the
59 behaviour of TRC material under thermomechanical condition. Some studies have investigated
60 the thermomechanical behaviour of carbon fabric-reinforced cementitious matrices [26,27], the
61 effects of continuous alkali-resistant (AR) glass textile on thermomechanical behaviour of TRC
62 glass (for temperatures ranging from 20 °C to 400 °C) [28], the effect of discontinuous glass
63 fibres charged in cementitious matrix on thermomechanical behaviour of a glass TRC (for
64 temperatures ranging from 20 °C to 600 °C) [29]. These studies allowed identifying evolution of
65 some thermomechanical characteristics (as ultimate stress, different stiffnesses defined from
66 stress-strain curve) of glass or carbon TRC as function of some parameters of composition of
67 cementitious matrix and of increasing temperature. Tlajji et al [30] recently studied
68 experimentally and comparatively thermomechanical and residual behaviours of AR glass TRC
69 subjected to elevated temperature loading. This previous study [30] showed that the effect of
70 cooling the composite after thermal loading below 220 °C is beneficial in terms of tensile
71 strength. This study also highlighted that under thermomechanical conditions, the ultimate stress
72 and the stiffness of the post-cracked composite of the AR glass TRC gradually decrease as the
73 temperature increases from 25 °C to about 150 °C, then gradually increase as the temperature
74 increases from about 150 °C to about 300 °C, then gradually reduce as the temperature (above
75 300 °C) increases. However, the thermomechanical tests, carried out in the previous study [30],
76 did not make it possible to obtain scientific explanations for experimentally identified results
77 related to the evolution of ultimate stress and the stiffness of the post-cracked composite of

78 glass TRC as function of increasing temperature. The purpose of the present paper is to deepen
79 scientific questions, asked after the previous study [30], thanks to physical, chemical and
80 thermomechanical characterisation.

81 To the best of the authors' knowledge, there have been no studies focusing on effect of the
82 nature of cementitious matrix on thermal and thermomechanical properties of glass TRC by
83 means of physiochemical and thermomechanical characterisation. This present paper provides
84 the scientific community the experimental data concerning thermal and thermomechanical
85 properties of TRC.

86 In the following sections of the present paper, composite configuration (section 2) and
87 experimental procedure (section 3) are presented. The experimental results will be then shown,
88 analysed (section 4) and discussed (section 5). This paper ends with a presentation of main
89 conclusions.

90 2 COMPOSITE CONFIGURATION

91 In this work, two textile-reinforced composites (3G.AR and 3G.AR.Fire) were manufactured
92 and studied. This section first presents the materials (matrices and fabrics) used to fabricate the
93 composite specimens, as well as their characterisation. Then, it presents the textile reinforced
94 concrete (TRC) preparation and specimen dimensions.

95 2.1 Matrices

96 Two different matrices were tested, namely normal mortar and refractory mortar. The matrices
97 used were commercial single-component cementitious repair mortars. They were made by
98 mixing water with a premixed powder at a water to powder (W/P) mass ratio of 0.18. The
99 rheology of the fresh cementitious matrices and the properties of the hardened cementitious
100 matrices after 28 days were experimentally identified (Table 1).

101

Properties of the cementitious matrix		Normal mortar			Fire mortar		
		Mean value	Number of tests	Standard deviation	Mean value	Number of tests	Standard deviation
Viscosity (or consistency) of the fresh mortar	Measurement of mortar flow table spread (cm) (Tests carried out according to the standard [31])	14	2	0.5	20	2	2
	Measurement of mortar viscosity using a plunger (cm) (Tests carried out according to the standard [31])	2	2	0	2.5	2	0.5
	Workability time (in second) of mortar subjected to mortar vibration (Tests carried out according to the standard [32])	28	2	2	12	2	0
Physical proprieties of the mortar	Control of entrained air volume (%) (Tests carried out according to the standard [31])	12	2	0	5	2	0
Mechanical proprieties of the hardened mortar	Compressive strength (MPa) after 28 days (Tests carried out according to the standard [32])	23.5	6	2.3	14.5	6	0.5
	Tensile strength (MPa) after 28 days (Strength obtained using flexural tests carried out according to the standard [32])	4.5	3	0.13	3.3	3	0.16

102

Table 1. Properties of the cementitious matrices

103 2.2 Fabrics

104 The only fabric reinforcement used in this work was alkali-resistant (AR) glass textile. The

105 physical and mechanical properties of a single fibre of the AR glass are presented in Table 2.

106 This type of glass textile was selected because of its excellent fire resistance (up to 860 °C) [33]
 107 and because it does not stretch and shrink after exposure to either extremely high or low
 108 temperatures [34]. The AR nature of the glass textile also exhibits an excellent capacity
 109 (compared to E-glass) to resist degradation in an alkaline environment. Other criteria that led to
 110 choose this type of reinforcement included nominal weight (g/m^2), mortar penetration ability,
 111 ease of cutting, and implementation conditions. The grid AR-glass textile used in this study had
 112 the same thread in two grid directions. Its mechanical properties are shown in Table 3. Its grid
 113 was large, with the opening between the mesh axes at 8×8 mm, which allows the passage of
 114 small aggregates.

Tensile resistance (MPa)	Elastic modulus (GPa)	Strain at (rupture (%))	Softening point (°C)	Poisson coefficient	Thermal expansion coefficient	Density (kg/dm^3)
1000–1700	74–76	1.8	860	0.25	7.9×10^{-6}	2.6

115 Table 2. Physical and mechanical properties of a single fibre of the alkali-resistant glass (supplier's data)

116

	Tensile strength	Elongation	Other characteristics				
	Warp/Weft direction	Warp/ Weft direction	Fibre diameter (μm)	Number of filaments/yarn	Yarn weight (Tex)	Nominal weight (g/m^2)	Grid mesh
AR Rovings Grid	25 kN/m	< 3%	19	1600	1200	300	8 mm \times 8 mm

118

119 Table 3. Mechanical properties of the grid AR-glass textile obtained from the supplier's technical data
120 sheet

121 2.3 Textile reinforced concrete

122 The composite processing technique and procedure, used for the fabrication of the 3G.AR and
123 3G.AR.Fire composites, have been established according to the recommendation of the RILEM
124 Technical Committee 232-TDT [35] that describes a standardized uniaxial tensile test method to
125 determine the load bearing behaviour of tensile specimens made of TRC. Hand lay-up moulding
126 was used for the fabrication of the 3G.AR and 3G.AR.Fire composites. This implementation
127 technique consisted of successively applying the mortar and the textile onto a wood mould
128 prepared in the laboratory. A thin fresh matrix layer was implemented with a trowel in the
129 mould and a grid textile layer was embedded within the matrix. Additional layers of matrix and
130 textile reinforcement were applied in the same way by ensuring good impregnation, and air
131 bubbles were eliminated as much as possible. The composites plate obtained was protected by a
132 plastic layer to avoid premature shrinkage and was stored in the laboratory in atmospheric
133 conditions. The manufacture of composite specimens is presented in detail in a previous study
134 [30].

135 After 7 days, the rectangular plates were demoulded and cut to obtain specimens of 700 mm ×
136 45 mm × 5 mm (length × width × thickness). The TRC materials (3G.AR and 3G.AR.Fire) were
137 made and kept in the laboratory under ambient conditions, and stored at ambient temperature for
138 at least one month before testing. To prepare each specimen for testing, four aluminium plates
139 were glued to the ends of each specimen using an epoxy adhesive to ensure transfer efficiency
140 of the mechanical load. At least 3 days after the bonding, each TRC sample (see Figure 1a) was
141 drilled at each end to be compatible with the “ball joint” loading heads used (see Figure 1b).

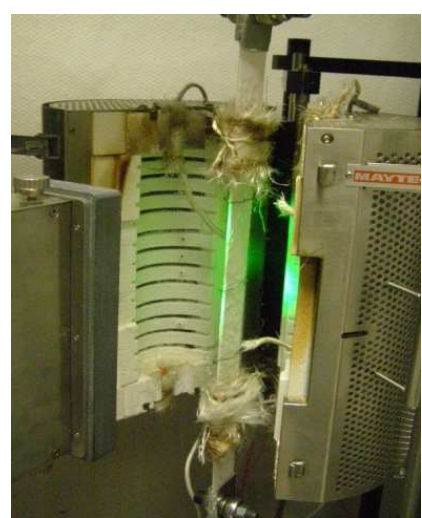
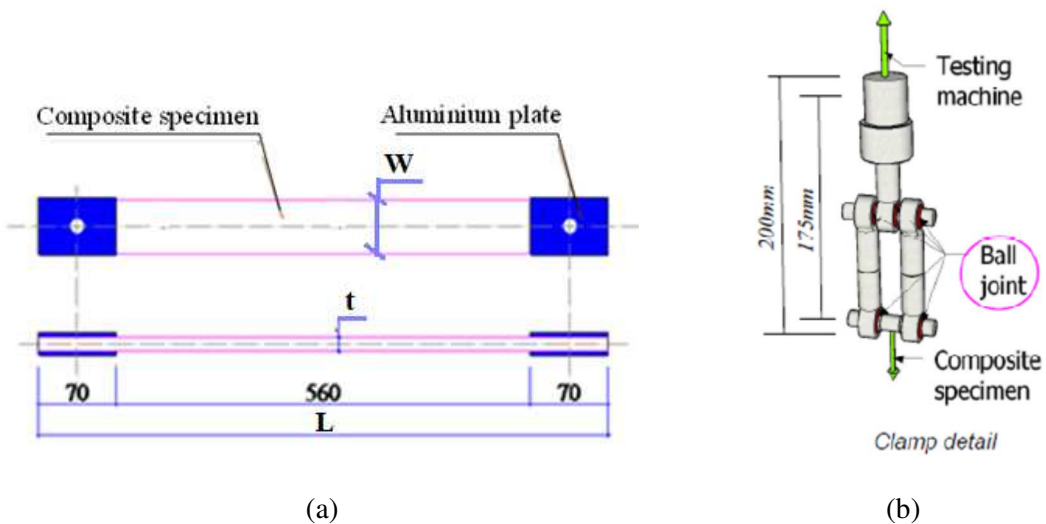
142 3 EXPERIMENTAL PROCEDURE

143 This section presents thermomechanical characterisation device, material thermomechanical
144 characterisation, material physical and mechanical characterisation.

145 3.1 Thermomechanical characterisation device

146 The thermomechanical machine (TM20kN-1200C) (Figure 1c) was used in this study to test
147 TRC specimens. It was fitted with a small furnace provided with heating resistors that can reach
148 a high temperature, potentially up to 1200 °C. This temperature is controlled by using integrated
149 thermocouples. The maximum rate of temperature rise in the furnace is 30 °C/min. The
150 specimen is placed in the middle of the furnace (Figure 1d), measuring 300 × 100 mm, and is
151 attached by two “ball joint” loading heads, designed in a previous study [36], which allow the
152 application of a tensile force and control of the alignment of the specimen.

153



154 Figure 1. (a) Composite specimen; t , w , L : thickness, width, length of the specimen.; (b) Used “ball joint”
 155 loading head; (c) Thermomechanical machine TM20kN-1200C; (d) furnace with specimen installed for a
 156 thermomechanical tensile test

157 3.2 Material thermomechanical characterisation

158 This section discusses the transient-state (TS) and steady-state (SS) tests used to characterise the
 159 thermomechanical behaviour of the TRC.

160 3.2.1 Transient-state (TS) test

161 In the TS tests, shown in Figure 2, the specimens were initially gripped at both ends and then
 162 subjected to a tensile force with a maximum load equal to a selected percentage of the

163 maximum strength of the TRC obtained at 25 °C (30% and 50%). The 30% σ_{UTS} (25°C) [or
164 50% σ_{UTS} (25°C)] represents a maximum tensile stress applied on TRC specimen that equals to
165 30% [or 50%] of the ultimate strength of TRC material tested at 25°C. Then, the temperature
166 was raised to the maximum that the TRC can resist. The same heating rate (30 °C/min) was
167 applied to specimen for all TS tests carried out.

168 To keep the load applied on the specimen constant throughout the test, the machine was
169 controlled using the test piloting software. The control was carried out according to the
170 following steps:

171 1) During heating from 25° C to failure temperature of TRC, the upper traverse of the
172 thermomechanical machine used (TM20kN-1200C) was always fixed.

173 2) During heating from 25°C to about 100°C, TRC expanded, the inferior traverse of the
174 machine moved down in order to compensate the thermal expansion of TRC.

175 3) During heating from about 100°C to the failure temperature of TRC, there was a thermal
176 shrinkage of TRC due to evaporation of water within TRC or other thermal effects, the inferior
177 traverse of the machine moved up in order to compensate the thermal shrinkage of TRC.

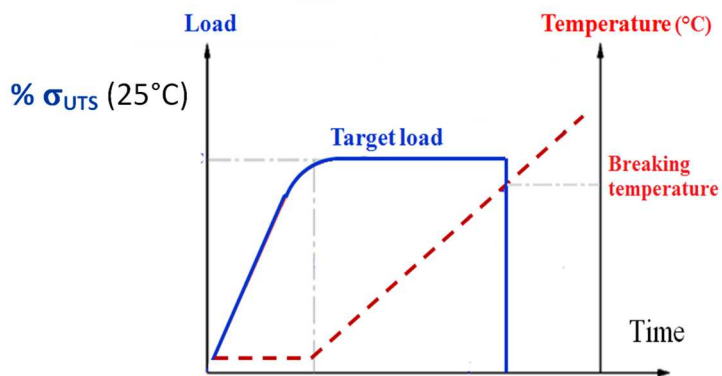
178 3.2.2 Steady-state (SS) test

179 In the SS test, shown in Figure 3, the specimens were heated to a specified temperature and then
180 loaded until failure while maintaining the same temperature. For the SS tests, because of
181 technological difficulties, the heating rate in the furnace during the temperature increase phase
182 is programmable and set as a function of the temperature level of the test, as recommended by
183 the manufacturer of the furnace to ensure its good operation and the homogeneity of the
184 temperature around the entire portion of the specimen placed in the furnace. All samples were
185 heat-treated by increasing the heating rate in the furnace (ranging from 2.5 °C/min to 20
186 °C/min) corresponding to each temperature level (ranging from 75 °C to 600 °C). When the
187 temperature reached the target value, it was kept constant for 1 h. The tensile force applied on
188 the specimen was piloted by displacement. It was monotonically increased with a rate of 3000

189 $\mu\text{m/m}$ to the maximum force (F_{max}) that the specimen could resist and then the ultimate axial
190 stress σ_{UTS} was calculated [$\sigma_{\text{UTS}} = F_{\text{max}}/(w*t)$; with t (thickness) and w (width) of the specimen
191 are defined in Figure 1a]. This mechanical load was combined with the measurement of the
192 axial strain of the specimen using a laser sensor. The tests and validation of the specimen
193 measurements obtained by the laser sensor have been previously described [28]. Figure 3
194 presents this test in terms of the evolution of temperature and force as a function of time. Table
195 4 shows the exploited tests performed on the 3G.AR and 3G.AR.Fire composites subjected to
196 steady-state tests.

Reference de TRC(*)	Dimensions of specimens (mm)	Test temperature (°C)	Heating rate (°C/minute)	Number of tests
3G.AR-25°C-1÷2	t=9 (±1) w=45(±1) L=700 (±10)	25	0	2
3G.AR-75°C-1÷3		75	2,5	3
3G.AR-150°C-1÷3		150	5	3
3G.AR-300°C-1÷2		300	10	2
3G.AR-400°C-1÷2		400	13	2
3G.AR-600°C-1÷2		600	20	2
3G.AR.Fire-25°C-1÷3		25	0	3
3G.AR.Fire-75°C-1÷3		75	2,5	3
3G.AR.Fire-150°C-1÷4		150	5	4
3G.AR.Fire-300°C-1÷4		300	10	4
3G.AR.Fire-400°C-1÷3		400	13	3
3G.AR.Fire-600°C-1÷2		600	20	2

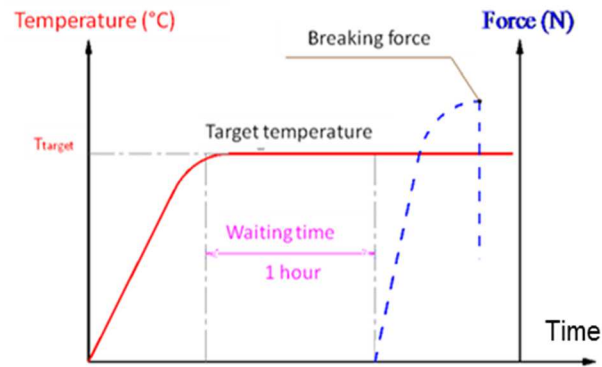
197 Table 4. Tests performed on the 3G.AR and 3G.AR.Fire composites; e, l, L: thickness, width,
198 length of specimen.



199

200

Figure 2. Transient-state path.



201

202

Figure 3. Steady-state path.

203 3.3 Material physical and mechanical characterisation

204 This section presents the micro-structural characterisation, TMA, chemical analysis, and TGA
 205 carried out on the two studied TRCs or their matrices.

206 3.3.1 Micro-structural characterisation

207 The samples were examined by X-ray tomography using a GE Phoenix v | Tome | Xs
 208 tomograph. The tomograph consists of an X-ray tube (transmitter), a digital detector, and a set
 209 of mechanical axes (support for the test piece) enclosed in a radioprotection cabin. “FIJI”
 210 software was used to drive the tomograph and reconstruct the tomographic images. The
 211 resolution depends strongly on the size of the sample and the power of the X-ray source. No
 212 pre-treatment was carried out on the samples. The volume of the samples, as observed by the
 213 tomograph, was $15 \times 15 \times 10 \text{ mm}^3$ (Figure 4). This size made it possible to have a resolution of
 214 $10 \mu\text{m}$ for observed samples, which is a priori sufficient for examining the fibre-matrix interface
 215 and the voids of the matrix. Using this technique, the fibres and voids in the composite can be
 216 observed without destroying the sample.

217 3.3.2 Thermomechanical analysis

218 TMA is the study of the relationships between a sample’s length (or volume) and its
 219 temperature. A thermomechanical analyser accurately measures the temperature of a sample, as
 220 well as very small movements of a probe in contact with the sample surface (Figure 5). A

221 Mettler Toledo TMA/SDTA 1 IC/600 instrument uses a quartz probe containing a thermocouple
222 for temperature measurement and it couples to the core of a linear variable differential
223 transformer (LVDT). The analysis was made on samples with a thickness of 5mm, heated with a
224 rate of 3°C/ minute.

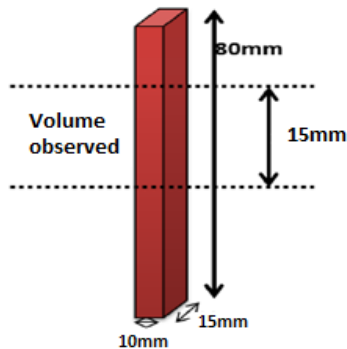


Figure 4. Volume observed by the tomograph.



Figure 5. Thermomechanical measurement

225 3.3.3 Chemical analysis

226 When water is present, the silicates and aluminates present in the mortar undergo hydration
227 processes, producing new hydrated compounds in the form of a jelly or crystals. The phases
228 forming the mortar are determined by X-ray diffraction and IR spectroscopy analysis in order to
229 compare the composition of the investigated mortars.

230 3.3.4 Thermogravimetric and differential thermal analyses (TGA-DSC)

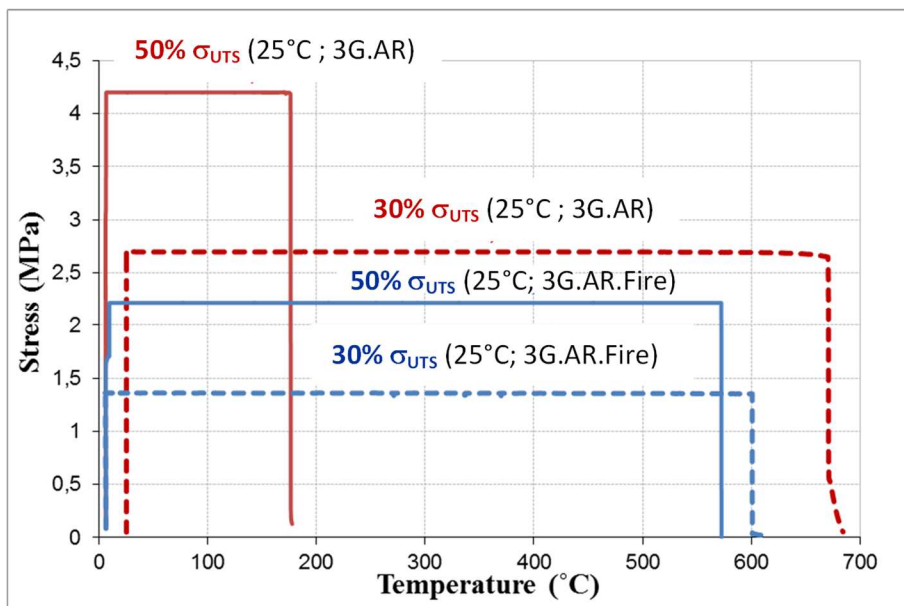
231 TGA measures the change in the mass of a material as a function of temperature and time in a
232 controlled atmosphere. However, DSC measures the heat flux associated with phase transitions
233 or reactions, such as dehydration, decarbonation, dihydroxylation, fusion, crystallization. The
234 most important products of the hydration reactions of ordinary cement are calcium silicate
235 hydrate (C-S-H) and calcium hydroxide, also called portlandite (CH) [37]. Different authors
236 have described the reactions that occur with increasing temperature in cement paste [38-43].
237 Simultaneous measurements of weight change (TGA) and heat flow (DSC) on a single sample
238 as a function of temperature or time were made by using a Mettler Toledo TGA-DSC3+
239 differential scanning calorimeter.

240 4 RESULTS

241 This section first shows the results of the transient-state tests, steady-state tests, tomography
242 observations, and thermal analyses (TMA, DSC) carried out on the two studied TRCs. It then
243 discusses the results of the chemical analysis (X-ray diffraction and IR spectroscopy) and TGA
244 carried out on mortars (or hardened matrices) of the two studied TRCs.

245 4.1 Results of transient-state tests of 3G.AR and 3G.AR.Fire

246 The failure temperature for each percentage of maximal strength obtained at 25 °C [30% σ_{UTS}
247 (25°C) and 50% σ_{UTS} (25°C)] was reached when the tensile load could no longer be sustained.
248 Figure 6 shows the temperature that causes failure of the specimens for 30% σ_{UTS} (25°C) and
249 50% σ_{UTS} (25°C) tension loads. In this figure, the horizontal axis represents the specimen
250 temperature and the vertical axis represents the load value. Table 5 represents the ultimate
251 temperature reached when TRC is subjected to the selected load.



252

253 Figure 6. Failure temperature of the specimens in the transient-state test.

254

	3G.AR		3G.AR.Fire	
	Load applied (MPa)	Ultimate temperature (°C)	Load applied (MPa)	Ultimate temperature (°C)
30% σ_{UTS} (25°C) (a)	2.6	670	1.3	600
30% σ_{UTS} (25°C) (b)	2.6	590 (*)	1.3	620
30% σ_{UTS} (25°C) (c)	2.6	672 (*)	/	/
50% σ_{UTS} (25°C) (a)	4.2	180	2.2	570
50% σ_{UTS} (25°C) (b)	4.2	185 (*)	2.2	545

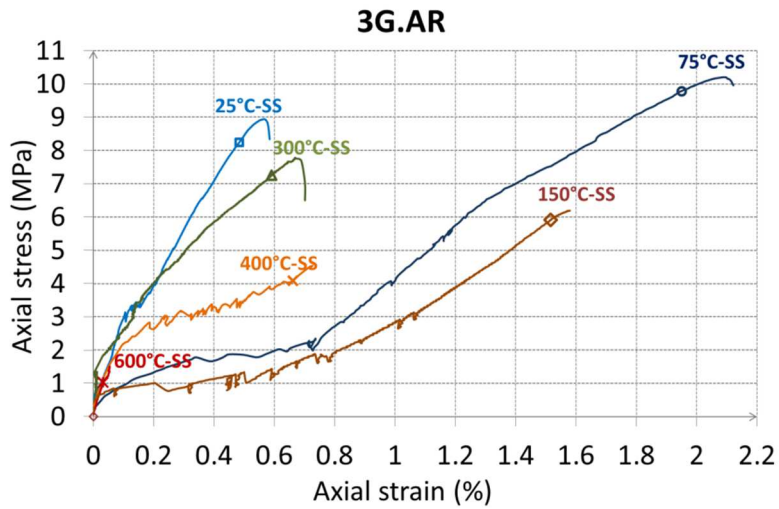
255 Table 5. Ultimate temperature reached for each stress; a, b, c: tests (a, b, or c) performed with the same
256 experimental condition on different specimens of the same TRC material; (*) results obtained by
257 NGUYEN et al. [44]

258 A sharp drop (of 72%) occurs in the failure temperature when the stress was increased from
259 30% σ_{UTS} (25°C, 3G.AR) to 50% σ_{UTS} (25°C, 3G.AR) for 3G.AR, whereas this decrease was
260 almost nil (5%) for 3G.AR.Fire (Table 4). This result shows the positive effect of the fire
261 (refractory) mortar used for 3G.AR.Fire, in comparison with the normal mortar used for 3G.AR.

262 4.2 Results of steady-state tests of 3G.AR and 3G.AR.Fire

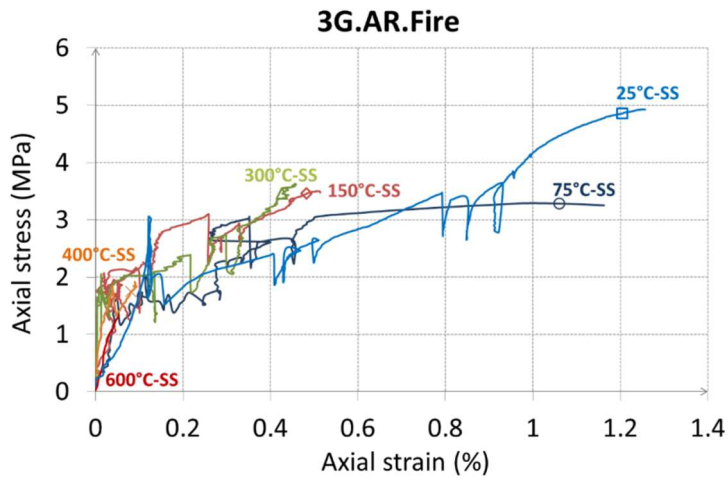
263 The influence of different temperatures on composite materials tested in this study is presented
264 in Figure 7a (for 3G.AR) and Figure 7b (for 3G.AR.Fire). Figure 7c provides a magnification of
265 the range between 0-0.4% axial strain of Figure 7b (for 3G.AR.Fire). The axial stress as a
266 function of the axial strain represents the behaviour of the TRCs at 25 °C, 75 °C, 150 °C, 300
267 °C, 400 °C, and 600 °C.

268



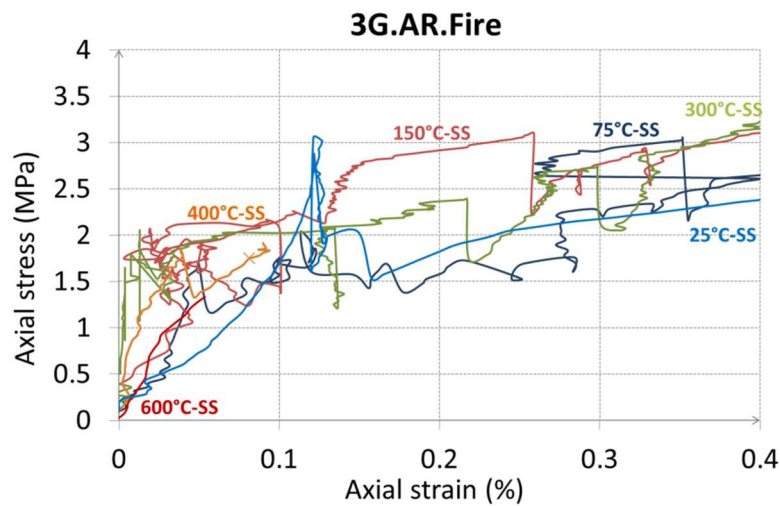
269
270

(a) Results of tests carried out on 3G.AR



271
272

(b) Results of tests carried out on 3G.AR.Fire



273
274

(c) Results of tests carried out on 3G.AR.Fire (magnification of the range between 0-0.4% strain)

275
276

Figure 7. Behaviour of (a) 3G.AR and (b,c) 3G.AR.Fire in steady-state tests: axial stress as a function of axial strain.

277 For 3G.AR (Figure 7a), the axial stress-axial strain curves at temperatures varying from 25 °C
278 to 150 °C show three distinguishable phases in the behaviour of the 3G.AR composite.
279 However, at 300 °C and 400 °C, two phases are observed. Additionally, at 600 °C, the curve is
280 quasi-linear, and only one phase is shown. However, the axial stress-axial strain curves of
281 3G.AR.Fire (Figures 7b,c) are disordered. This composite shows nearly the same behaviour at
282 all temperature levels; only the ultimate strength changes.

283 Steady state tests of normal mortar based TRC (3G.AR) (Figure 7a) show distinct phases of
284 deformation progression with increasing tensile loading. However, the tensile stress-strain
285 curves of 3G.AR.Fire (Figure 7b) are less clear than that those of 3G.AR. The difference
286 between the stress-strain curves of 3G.AR (Figure 7a) and of 3G.AR.Fire (Figure 7b) can be
287 explained by the following reasons:

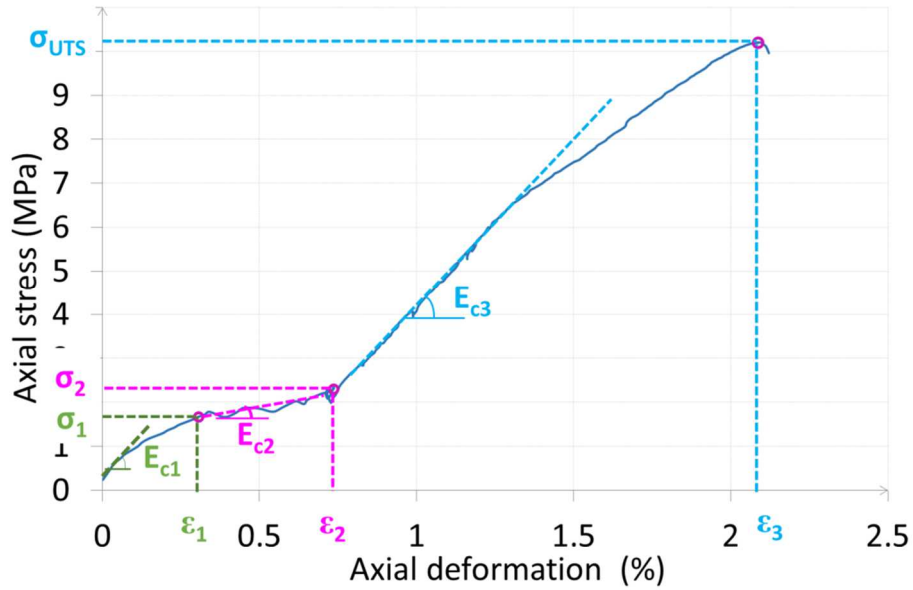
288 a) For a same axial stress level, the axial strain of 3G.AR.Fire is greater than that of 3G.AR
289 and the stiffness of 3G.AR.Fire is lower than that of 3G.AR because the room
290 temperature tensile strength of the normal matrix of 3G.AR is greater than that of the fire
291 matrix of 3G.AR.Fire of 30%.

292 b) The particle size of the matrix influences the interaction between the textile and the
293 matrix. The particle size of the normal matrix is finer than that of the fire matrix (according
294 to tomographic observation presented in Figure 12), which leads to a better interaction
295 between the textile and the matrix within 3G.AR. This is reflected in the transfer of load
296 (mortar / textile) and finally in the evolution of the curve. In addition, the measurement of
297 axial strain of TRC, a non-contact measurement method given by the laser sensor, is
298 influenced by rough level of the measurement surfaces and the particle size of the matrix of
299 TRC. The dimensions of the fine aggregates of the fire mortar are greater than those of the
300 normal mortar, as seen by tomographic observation in Figure 12, which causes an imperfect
301 cohesion between the particles of the matrix and at the matrix-textile interface. This
302 contributes to explain, at least partially, the variability of the stress/strain curves of
303 3G.AR.Fire specimens, shown in Figures 7b and 7c.

304 The average slopes of the third phase of the stress/strain curves of both TRCs (after cracking of
305 the matrix) are mainly dependent on the behaviour of glass textiles and less dependent on the
306 particle size of the matrix. This contributes to explain why the third phase of each stress/strain
307 curve of 3G.AR.Fire (for each temperature level) is clearer than the first and second phases of
308 the same curve (see Figure 7b). For this reason, in the following of this paper, the comparison
309 between the tensile behaviours of 3G.AR and 3G.AR.Fire is carried out for two important
310 parameters [average ultimate tensile strength (σ_{UTS}) and average post-cracked composite
311 stiffness (E_{c3})], which are less sensitive to the singularities of macroscopic curves, that can be
312 identified from the last phase of the stress/strain curves (after cracking of the matrix).

313 From the curves presented in Figure 7a and b, the mechanical properties of the two studied
314 composites can be identified as shown in Figure 8. The methodology presented in Fig. 8 for
315 calculating the ultimate tensile strength (σ_{UTS}) and the ultimate stiffness (E_{c3}) was applied for
316 each of the curves of Figure 7a (for 3G.AR) and Figure 7b (for 3G.AR.Fire). The value of the
317 average slope of the third phase of each stress-strain curve (shown in Figure 7a and Figure 7b)
318 represents the ultimate stiffness value E_{c3} of the corresponding composite for each temperature
319 level.

320 In order to determine, as correctly as possible, the ultimate tensile strength (σ_{UTS}) and the
321 ultimate stiffness (E_{c3}), many steady-state tests have been carried out in the same experimental
322 conditions for each material (3G.AR or 3G.AR.Fire) and each temperature level. The exploited
323 steady-state tests performed on the 3G.AR and 3G.AR.Fire composites were synthesized in
324 Table 4. This allowed to determine the evolution of average values (with error bars showing
325 standard deviations) of the ultimate tensile strength (σ_{UTS}) and the ultimate stiffness (E_{c3}) for
326 each material (3G.AR or 3G.AR.Fire) and each temperature level (as shown in Figure 9 for σ_{UTS}
327 and in Figure 10 for E_{c3}).



328

329

Figure 8. Identification of mechanical properties of TRC

330 σ_1 : Composite macro-cracking stress; E_{c1} : initial stiffness of the composite before macro-
 331 cracking; ϵ_1 : axial strain in phase 1; σ_2 : stress level of the composite corresponding to phase 2;
 332 E_{c2} : stiffness of the cracking phase; ϵ_2 : axial strain in phase 2; σ_{UTS} : ultimate stress level of the
 333 composite corresponding to the breaking force; E_{c3} : stiffness of phase 3 (or stiffness of the post-
 334 cracked composite); and ϵ_{UTS} : maximum thermomechanical axial strain.

335

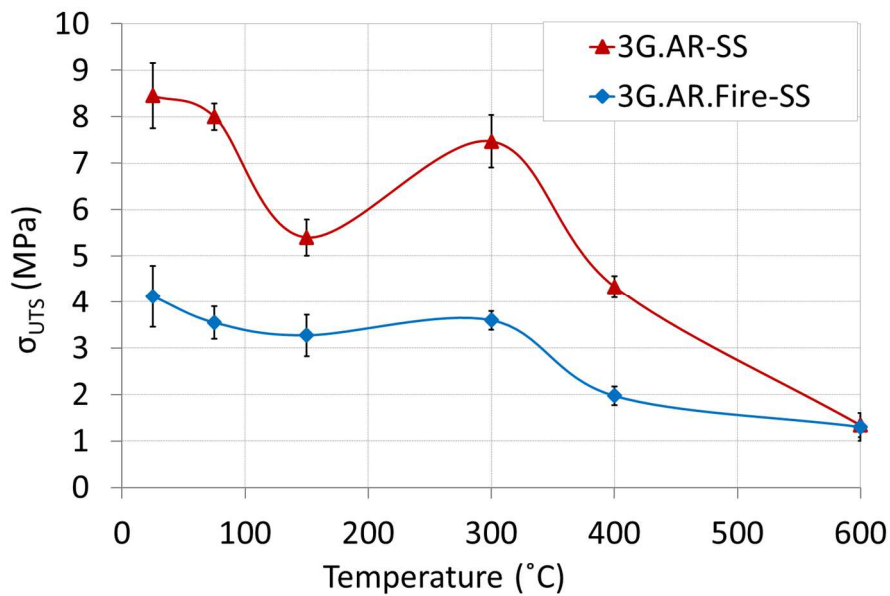
336 Table 5 displays the experimental values of average ultimate tensile strength (σ_{UTS}) and the
 337 average post-cracked composite stiffness (E_{c3}) of 3G.AR and 3G.AR.Fire composites at
 338 different temperatures varying from 25°C to 600°C (the standard deviation values are written in
 339 parallel).

340

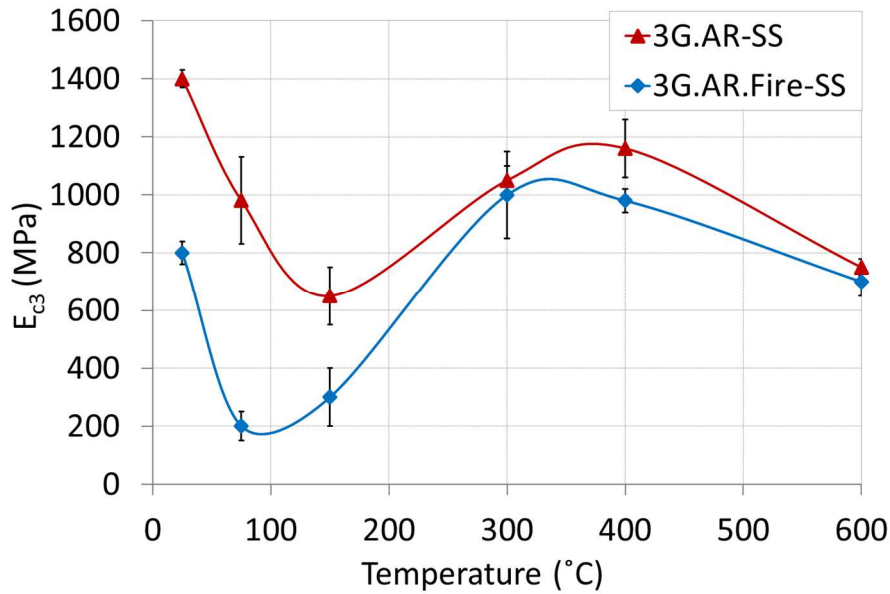
T°C	3G.AR		3G.AR.Fire	
	σ_{UTS}	E_{c3}	σ_{UTS}	E_{c3}
	(MPa)	(GPa)	(MPa)	(GPa)
25	8.45 (0.70)	1400 (30)	4.2 (0.6)	800 (40)
75	8 (0.28)	980 (150)	3.5 (0.35)	200 (50)
150	5.4 (0.39)	650 (100)	3.3 (0.4)	300 (100)
300	7.5 (0.57)	1050 (50)	3.6 (0.2)	1000 (150)
400	4.3 (0.23)	1160 (100)	1.9 (0.2)	980 (40)
600	1.3 (0.26)	750 (30)	1.3 (0.3)	700 (50)

341 Table 5: Results of the steady-state tests performed on 3G.AR and 3G.AR.Fire composites at different
342 temperatures (the standard deviation values are written in parallel)

343 The evolutions of the average ultimate tensile strength (σ_{UTS}) and stiffness (E_{c3}) as a function of
344 temperature are presented in Figure 9 and Figure 10, respectively, for both composite materials;
345 these two composites have almost the same rate of reinforcement ($V_f = V_{fibres}/V_{composite} = 2\%$).



346
347 Figure 9. Average ultimate tensile strength (σ_{UTS}) of 3G.AR and 3G.AR.Fire as a function of temperature.



348

349 Figure 10. Average ultimate stiffness (E_{c3}) of 3G.AR and 3G.AR.Fire as a function of temperature.

350 A comparison of 3G.AR and 3G.AR.Fire (Figure 9) shows that the resistance, when measured
 351 as a function of temperature levels, is higher in 3G.AR, whereas the maximum strength
 352 decreases by approximately 84% for 3G.AR and by approximately 69 % for 3G.AR.Fire when
 353 the temperature level changes from 25 °C to 600 °C. For each temperature level below 600°C,
 354 the ultimate strength of 3G.AR.Fire is lower than that of 3G.AR (Figure 9) because both
 355 compressive and tensile strengths of the normal mortar are noticeably lower than those of the
 356 fire mortar (see Table 1). It can be seen from Figure 9 that the resistance decreases between 25
 357 °C and 120 °C, whereas it increases between 120 °C and 300 °C.

358 Figure 10 shows that when the temperature level increases from 25 °C to 80 °C (for
 359 3G.AR.Fire) or 120°C (for 3G.AR), the stiffness E_{c3} of these composites progressively decrease.
 360 From the last temperature value (80 °C for 3G.AR.Fire or 120°C for 3G.AR) up to about 350°C,
 361 the stiffness E_{c3} of these composites progressively increase. For temperature levels above 350
 362 °C, the stiffness E_{c3} of these composites gradually decreases.

363 To explain the difference in behaviour between 3G.AR and 3G.AR.Fire (see Figure 9 and
 364 Figure 10), the identification of the physical and chemical properties of these two materials was
 365 proceeded by the material characterization methods shown in the sections 3.3.2, 3.3.3 and 3.3.4.

366 4.3 Failure modes

367 The observations after the tests (Figure 11) showed ruptures of 3G.AR and 3G.AR.Fire
368 specimens at each temperature (25 °C, 75 °C, 150 °C, 300 °C, 400 °C and 600 °C).



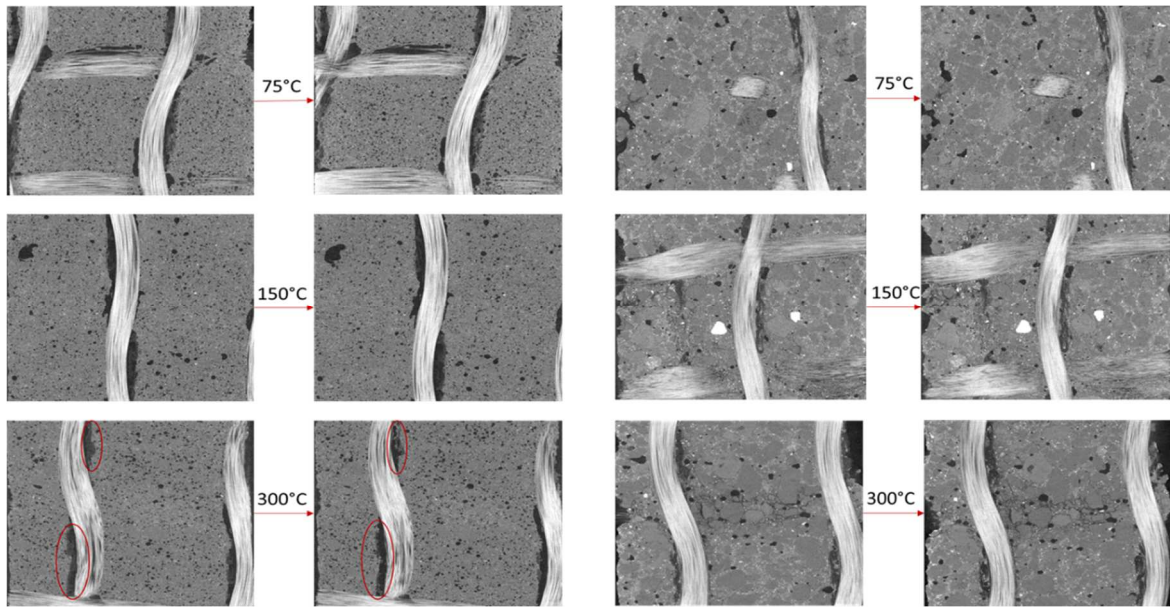
370 Figure 11. Failure modes of 3G.AR and 3G.AR.Fire at different temperatures

371 All specimens have a rupture characterized by a macro crack that is almost perpendicular to the
372 direction of the tensile load. For tests at 25°C, the failure occurred in TRC material and was
373 close to loading heads because there was a stress concentration at the vicinity zone between the
374 ends of the specimen and the reinforced aluminium plates. The failure mode of TRC, subjected
375 to uniaxial tension at 25° C, is consistent with what has been observed and discussed in previous

376 studies [28,36]. While the temperature increases from 75°C to 600°C, the macro crack is
377 systematically located in the submerged zone of the specimen in the furnace. This changes the
378 location of the failure zone of the specimen. Due to the effect of temperature, after matrix
379 damage and the consequent degradation of the matrix/textile interface that ensured load transfer,
380 the glass textile yarns ruptured when the tensile load exceeded their resistance thresholds, which
381 led to the rupture of the specimen. The rupture of the glass textile yarns is followed by an
382 opening of the lips of the macro crack in the middle of the sample.

383 4.4 Results of tomography observations

384 The results of the X-ray analysis are presented as grey-level images. Figure 12 shows different
385 raw images for 3G.AR (Figure 12a and b) and 3G.AR.Fire (Figure 12c and d). The reference
386 specimens (Figure 12a for 3G.AR and Figure 12c for 3G.AR.Fire) correspond to the non-
387 preheated samples of the composite. Each reference specimen was then preheated each time to
388 the temperature levels of 75 °C, 150 °C, and 300 °C and progressively cooled to 25 °C. These
389 experimental tests were carried out for temperatures up to 300° C in order to better deepen the
390 phenomena that lead to significant evolution, between 75°C and 300°C, of the average ultimate
391 tensile strength (σ_{UTS}) (Figure 9) and the average post-cracked stiffness (E_{C3}) (Figure 10) of both
392 TRCs. Using these images, the fibres and the matrix can be distinguished at different
393 temperature levels based on the differences in their grey levels.



394

395

(a)

(b)

(c)

(d)

396

Figure 12. Raw images of (non-preheated) reference specimens of (a) 3G.AR and (c) 3G.AR.Fire; raw

397

images of preheated-cooled specimens (preheated at 75 °C, 150 °C, or 300 °C) of (b) 3G.AR and (d)

398

3G.AR.Fire.

399

Figure 12a, b, c, and d show that no differences are observed between the raw image of (non-

400

preheated) reference specimens and those of the preheated-cooled specimens for both 3G.AR

401

and 3G.AR.Fire. Only a disappearance of the grey zone between the fibres and the matrix of the

402

TRC 3G.AR treated at 300 °C is observed. This phenomenon corresponds to the degradation of

403

the matrix resulting from its chemical decomposition or the transformation of one hydrate from

404

the matrix to another. Therefore, a physical and chemical analysis (cf. Sections 4.5, 4.6 and 4.7)

405

was carried out to understand the mechanisms that occur within the normal mortar and the fire

406

mortar.

407

4.5 Thermomechanical analysis

408

The difference in the behaviour of TRC (subjected to temperatures between 25 °C and 300 °C)

409

can also be related to the deformation of TRC subjected to thermal load. Figure 13 shows the

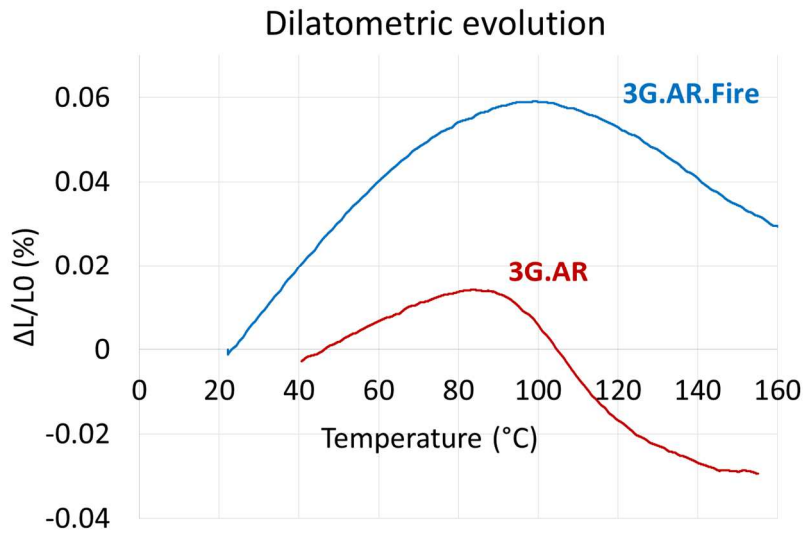
410

deformation of 3G.AR and 3G.AR.Fire as a function of temperature. This result from TMA is

411

presented for temperatures up to 150 °C in order to better understand the phenomena that lead to

412 significant evolution of the average ultimate tensile strength (σ_{UTS}) (Figure 9) and the average
413 post-cracked stiffness (E_{C3}) (Figure 10) of both TRCs.



414

415 Figure 13. Deformation of 3G.AR and 3G.AR.Fire as a function of temperature.

416 Figure 13 shows that from 25 °C to approximately 100 °C for 3G.AR.Fire and from 40 °C to
417 approximately 85 °C for 3G.AR, there is a marked expansion in the two materials. This step
418 corresponds to a substantial release of water, creating porosity. From 85 °C (for 3G.AR) or 100
419 °C (for 3G.AR.Fire) to 150 °C, both materials present a slight shrinkage. The mechanical
420 ultimate strength σ_{UTS} and stiffness E_{C3} of the material generally decreases between 25 °C and
421 150 °C (see Figure 9 and Figure 10) because of the different dehydration reactions that are
422 responsible for multicracking. However, between 150 °C and 300 °C (see Figure 9), with water
423 molecules released, the hydration of anhydrous cement particles occurs. The material undergoes
424 a small shrinkage and the micro-cracks close, resulting in a gain in strength and stiffness when
425 the temperature increases from 150 °C to 300 °C (see Figure 9 and Figure 10).

426 4.6 X-Ray diffraction and IRTF spectroscopy analysis

427 The phases composing the mortar were determined by X-ray diffraction and IRTF spectroscopy
428 analysis in order to compare the composition of the investigated mortars. X-ray diffraction
429 allows identification of the well crystallized mineral phases. IRTF spectroscopy completes the

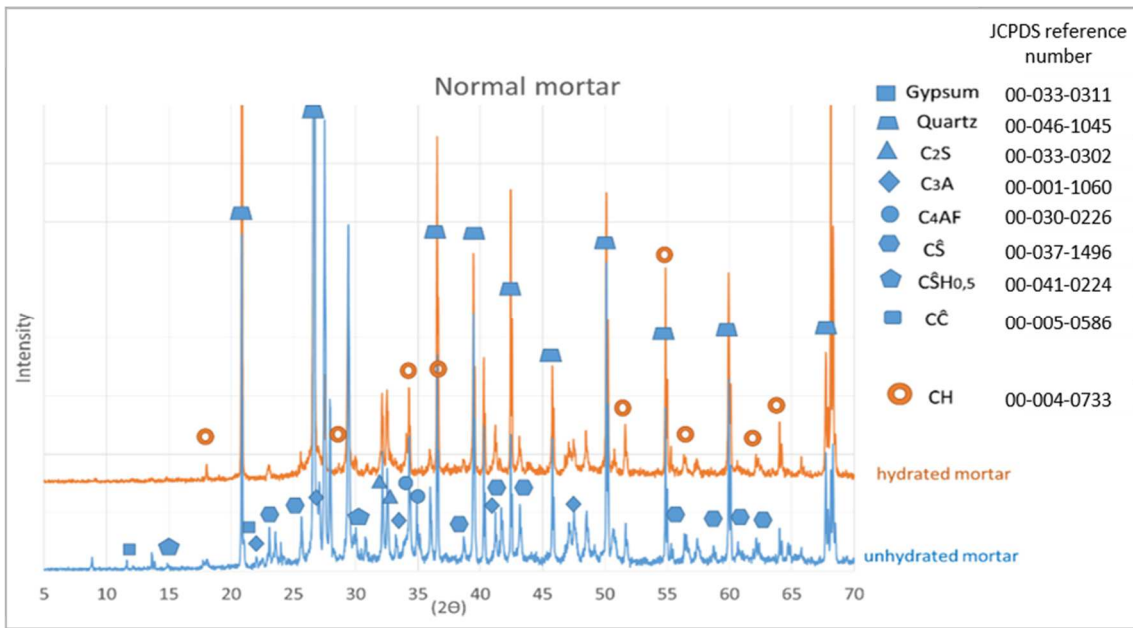
430 information derived from X-ray diffraction on poorly crystallized elements. The characterisation
431 of the powders of normal mortar (3G.AR) (see Figures 14, 15a,b) shows the presence of basic
432 phases of Portland cement: silicate phases (alite C_3S , belite C_2S); aluminate phases (C_3A ,
433 C_4AF), and sulfate phases ($C\hat{S}H_{0.5}$, $C\hat{S}H_2$, $C\hat{S}$). Although the fire mortar (of 3G.AR.Fire) (see
434 Figures 16, 17a,b) contains the basic elements of aluminous cement (CA , $C_{12}A_7$, C_3A), it also
435 contains the silicate phase (belite C_2S), anhydrite ($C\hat{S}$), and ferrite phase (C_3FT). The
436 correspondence between the anhydrous and hydrated patterns of the two mortar samples is
437 depicted in Figure 14 and Figure 15a and b for normal mortar and in Figure 16 and Figure 17a,
438 b, and c for fire mortar. The hydration of these mortars occurs mainly with silicates on one hand
439 and between the aluminates and sulphate phases on the other hand. This hydration leads to the
440 formation of a variety of hydrates, which can be seen with XRD and IRTF spectroscopy
441 analysis. Calcium monosulfoaluminate (Afm), C-S-H, and portlandite (CH) are the basic
442 hydrated phases of a normal mortar (see Figure 15a and b). Although portlandite (CH) does not
443 exist in the fire mortar, the presence of C-S-H can be detected in Figure 17a and b. The presence
444 in excess of aluminate causes the formation of stable phases of Calcium monosulfoaluminate
445 (Afm), stratlingite (C_2ASH_8) and gibbsite (AH_3) (see Figure 17a, b and c).

446

447

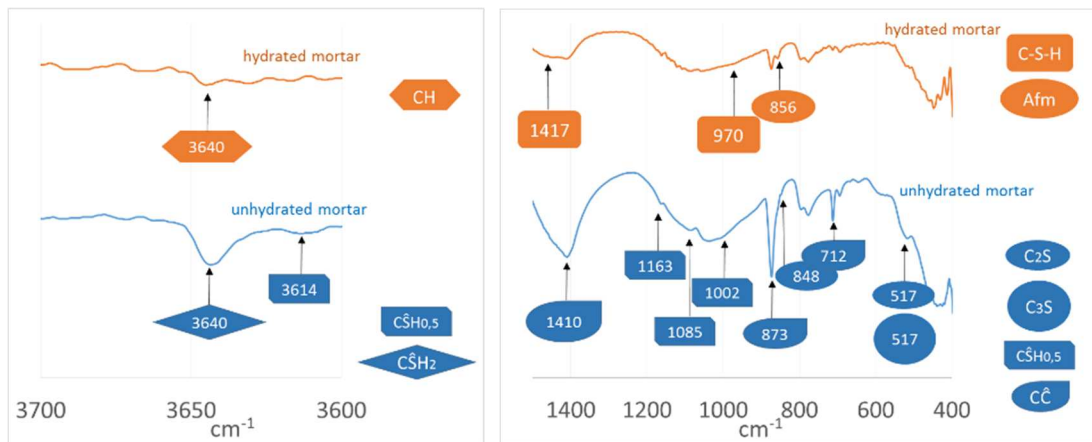
448

449



450

451 Figure 14. X-ray diffractometry of unhydrated and hydrated normal mortar (of 3G.AR); JCPDS reference
452 number: "Joint Committee on Powder Diffraction Standards" reference number.



453

454

(a)

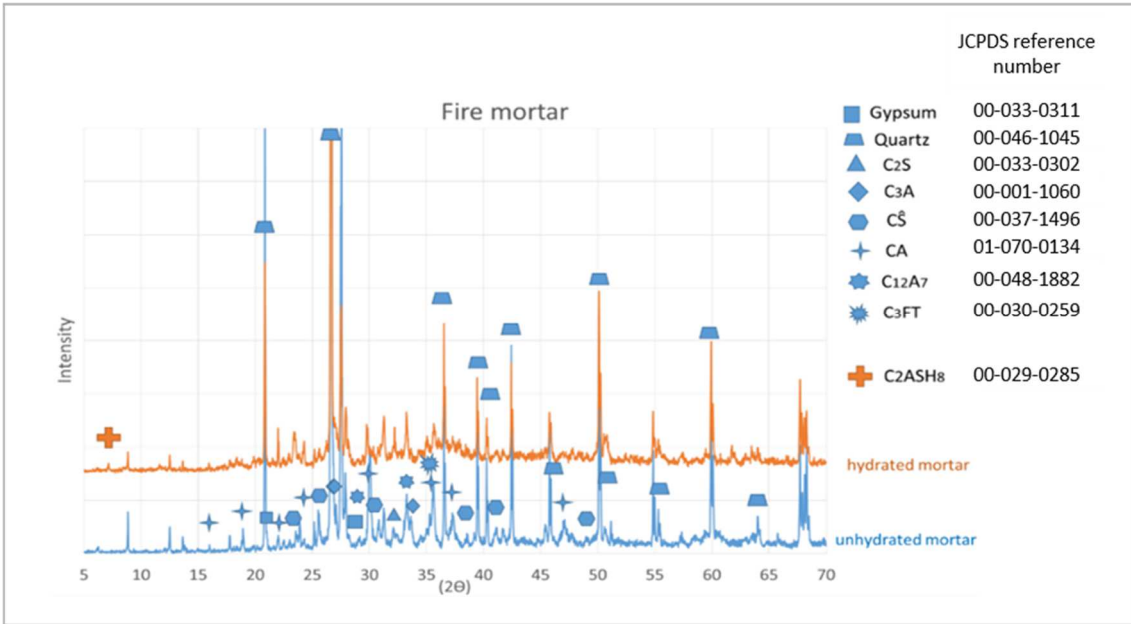
(b)

455 Figure 15. IR spectrum of unhydrated and hydrated normal mortar (of 3G.AR);

456

(a) between 3700 cm^{-1} and 3600 cm^{-1} , (b) between 1450 cm^{-1} and 400 cm^{-1} .

457



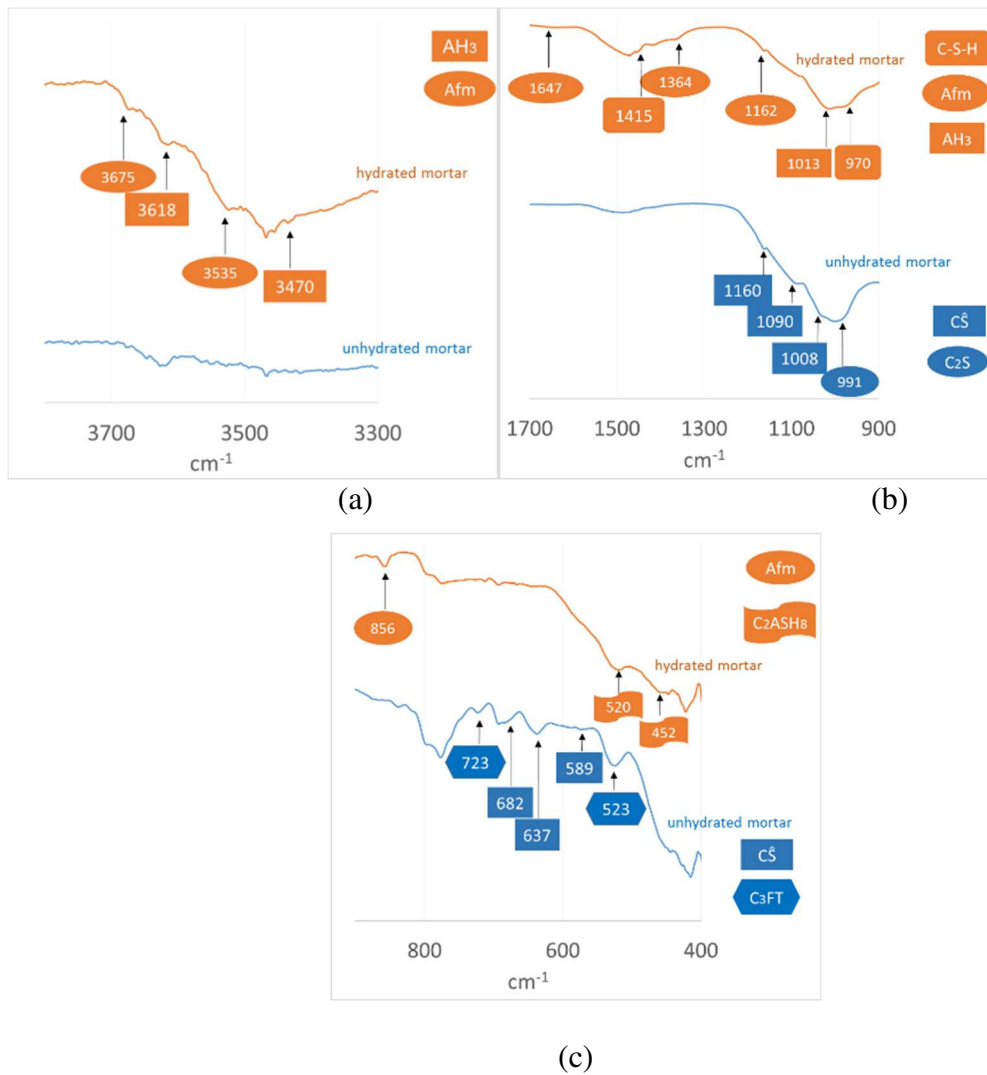
459

460

461

462

Figure 16. X-ray diffractometry of unhydrated and hydrated fire mortar (of 3G.AR.Fire); JCPDS reference number: "Joint Committee on Powder Diffraction Standards" reference number.



463
464

465

466

467

468

469

Figure 17. IR spectrum of unhydrated and hydrated fire mortar (of 3G.AR.Fire); (a) between 3700 cm^{-1} and 3300 cm^{-1} , (b) between 1700 cm^{-1} and 900 cm^{-1} , (c) between 900 cm^{-1} and 400 cm^{-1}

4.7 Thermogravimetric analysis

470

471

472

473

474

475

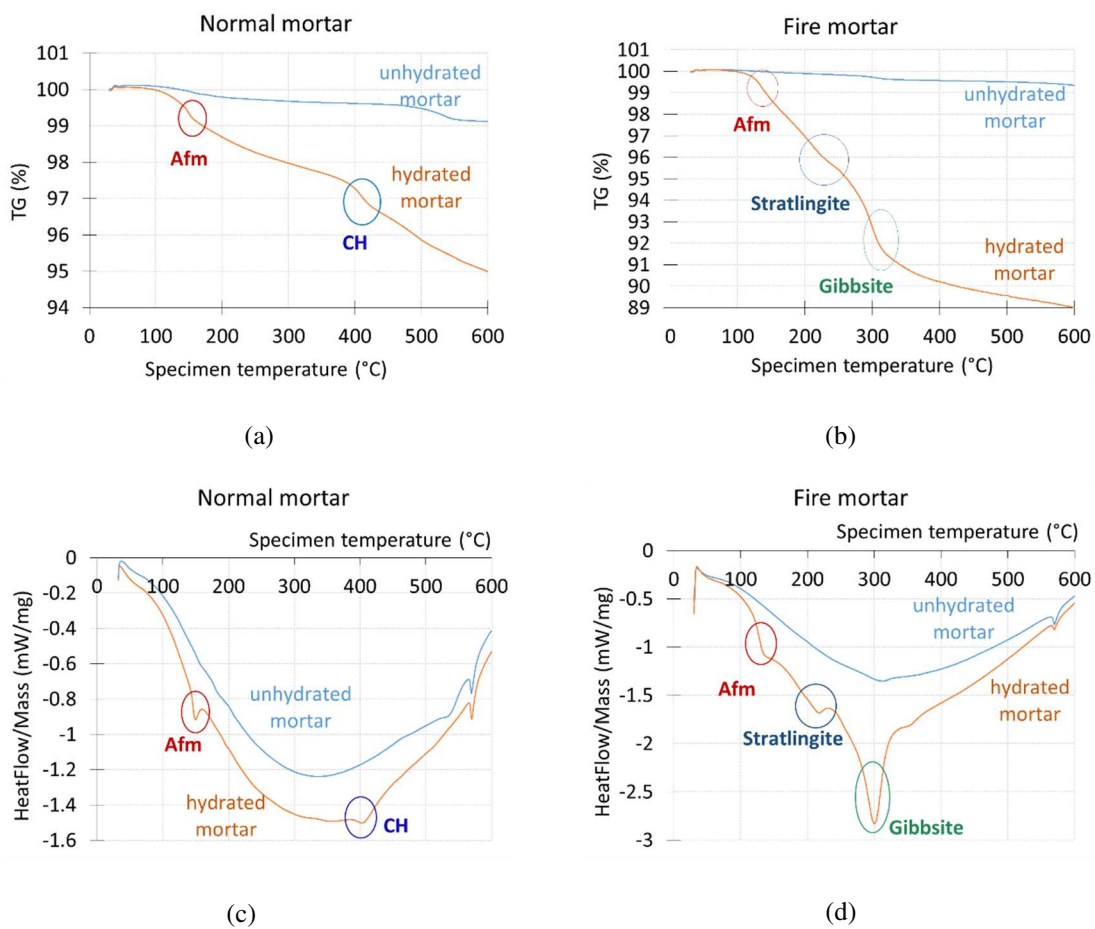
476

477

TGA was performed in order to understand the mechanisms that occur within normal mortar (of 3G.AR) and fire mortar (of 3G.AR.Fire) as a function of temperature. Upon heating, with a rate of 10°C/minute, the cement paste undergoes a continuous sequence of more-or-less irreversible decomposition reactions. In order to perform TGA on the mortars, the mortars were crushed into powder. The powder mass of the specimens used for TGA and DSC is about 20 mg.

First, TGA and DSC analyses were performed on the unhydrated and hydrated mortar powder (see Figure 18a and c for the normal mortar and Figure 18b and d for the fire mortar). It shows that the first weight loss located at 150 °C for both mortars is the result of dehydration reactions

478 of calcium monosulfoaluminate (Afm) and can be accompanied by dehydration of C-S-H (see
 479 Figure 18a and b). For the fire mortar, a difference between 200 °C and 250 °C was observed
 480 (Figure 18b and d), which corresponds on the decomposition of stratlingite. Moreover, this peak
 481 does not exist in the normal mortar (see Figure 18a and c), and the dihydroxylation of gibbsite is
 482 observed in the fire mortar (see Figure 18b and d). At 400 °C, dihydroxylation of portlandite
 483 (CH) occurred; portlandite was present in the normal mortar (see Figure 18a and c), but not in
 484 the fire mortar (see Figure 18b and d).
 485

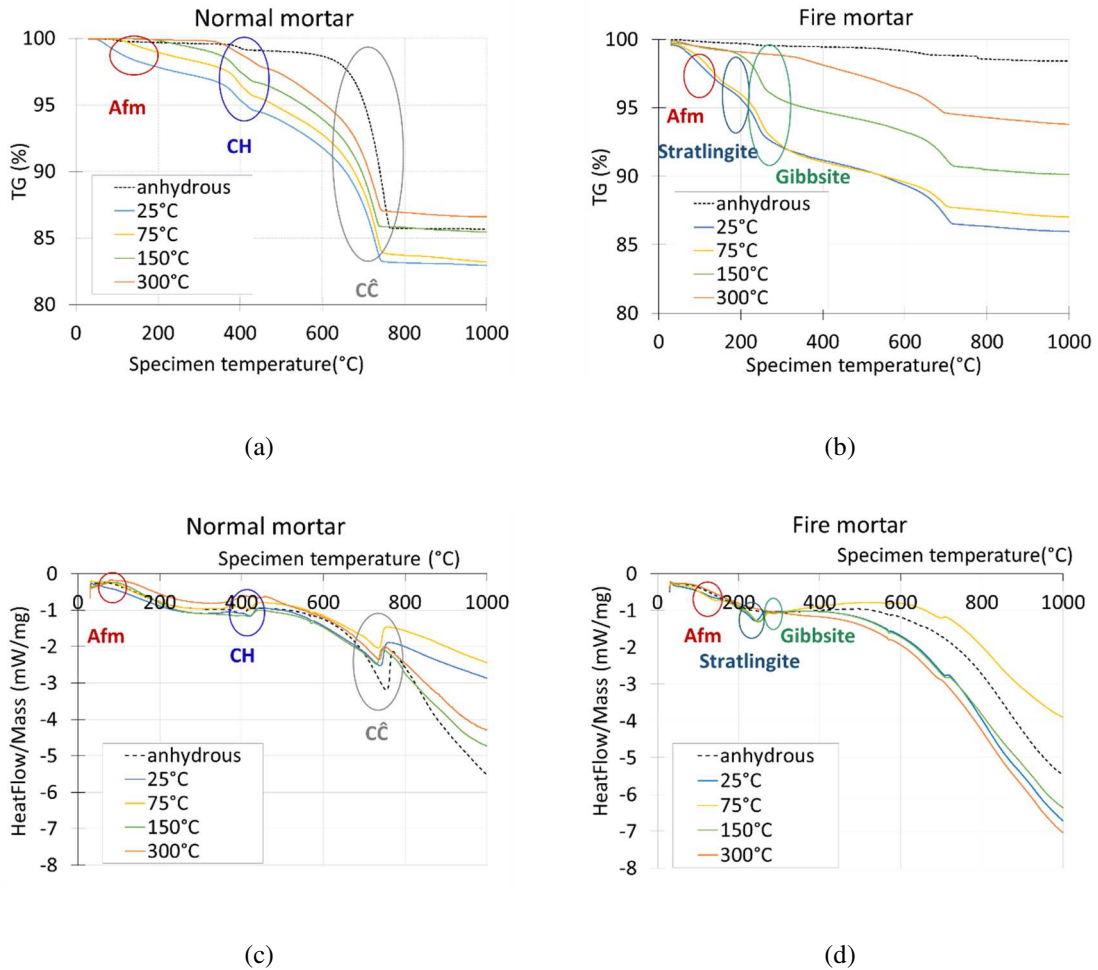


486 Figure 18. Detailed TGA and DSC analyses of hydrated and unhydrated for normal mortar (a, c) and fire
 487 mortar (b, d).

488 After identifying the phases of mortar by heating the powder to 600 °C, the effect of different
 489 temperature levels (25 °C, 75 °C, 150 °C, and 300 °C) on the mineralogical composition of

490 mortar hydration products was investigated. The TGA results for the normal mortar and fire
 491 mortar samples, previously preheated at different temperature levels (25 °C, 75 °C, 150 °C, and
 492 300 °C), are summarized in Figure 19.

493



494 Figure 19. TGA and DSC results of the preheated-cooled normal mortar (of 3G.AR) (a, c) and preheated-
 495 cooled fire mortar (of 3G.AR.Fire) (b, d). TGA and DSC tests: performed on mortar samples previously
 496 preheated at different levels of temperature and cooled to ambient temperature.

497 A comparison between the curves representing the preheated-cooled cement paste at different
 498 temperatures reveals that the amount of hydrates decreases with increased temperature and
 499 disappears for the preheated (at 300 °C)-cooled samples for both the normal mortar (see Figure
 500 19c) and the fire mortar (see Figure 19d). The results show that the samples preheated to 300 °C

501 do not present any weight loss (see Figure 19a and b) and the corresponding heat flow peak (see
502 Figure 19c and d) before 300 °C. All hydrates (Afm, stratlingite, and gibbsite) decomposed
503 before this temperature level. In contrast, portlandite (CH), which existed in the normal mortar
504 (see Figure 19a and c) and not in the fire mortar (see Figure 19b and d), decomposes between
505 400 °C and 450 °C and always appears in the sample preheated to 300 °C (Figure 19a and c).
506 Recrystallization of silica occurs at 580 °C for both mortars, and the decarbonation of calcium
507 carbonate (CC) occurs at 700 °C for normal mortar.

508 5 DISCUSSION

509 This experimental study enabled a comparison between the behaviour of 3G.AR and
510 3G.AR.Fire and identification of the effect of the cementitious matrix nature. It is observed that
511 the resistance as a function of temperature levels is higher in 3G.AR. This is due to the
512 resistance of the normal matrix which is greater than that of the fire matrix and on the other
513 hand, after a tomographic observation (Figure 12), to the physical state of the matrix. The
514 dimensions of the fine aggregates of the fire mortar are greater than those of the normal mortar,
515 as seen by tomographic observation in Figure 12, which causes an imperfect cohesion between
516 the particles of the matrix and at the matrix-textile interface.

517 The second point discussed in this study is that the behaviour of the TRC composites tested as a
518 function of temperature and specifically the reduction of the resistance between 25 ° C and 150
519 ° C and its increase between 150 ° C and 300 ° C (Figure 9 and Figure 10). This behaviour is
520 justified after chemical and thermal analyses. The TRC resistance and elastic modulus are
521 related to the porosity. Well crystallized and dense materials showed the highest mechanical
522 strength.

523 The TRC mechanical strength drops during the cement conversion step, between 25 ° C and 120
524 ° C [15,16]. In this temperature interval, water molecules are released by the dehydration of the
525 calcium monosulfoaluminate (Afm) and C-S-H phases (Figure 18). A thermomechanical
526 analysis on the dilatometric evolution of the mortar shows an expansion in this temperature
527 interval (Figure 13), which is responsible for the progression of micro cracks. This phenomenon

528 causes an increase in porosity and then a decrease in the resistance. However, between 150°C
529 and 300°C with the water molecules released, the hydration of the anhydrous particles of
530 cement occurs, especially in the aluminate phases (CA, C₃A, C₄AF and C₁₂A₇) that are present
531 in the fire mortar more than in the normal mortar. Stable phases appear again (as AH₃ and
532 C₂ASH₈), the material undergoes a small thermal shrinkage and the micro cracks close, which
533 results in a gain in strength and stiffness. This formation of stable hydrates explains the more
534 resistance stability of 3G.AR.Fire between 25 °C and 300 °C, compared to that of 3G.AR
535 (Figure 9). For temperature levels above 300°C, the TRC material is strongly damaged by the
536 temperature effect, the ultimate stress (see Figure 9) and the stiffness E_{c3} (see Figure 10)
537 progressively decrease when temperature increases.

538 The thickness of TRC has an influence on the behaviour of TRC in the transient-state loading
539 path. With a same applied mechanical load level in the transient-state tests and a same thickness
540 for both TRCs, the 3G.AR.Fire has a better thermal stability than the 3G.AR (see Figure 6 and
541 Table 5). This shows that the thermal diffusivity of the normal mortar is greater than that of the
542 fire mortar. When the thickness of the TRC with refractory matrix is greater, the thermal
543 stability of this TRC will be more significant.

544 6 CONCLUSION

545 This paper presents physical and chemical and thermomechanical characterisation of two glass
546 TRC for studying and deepening the understanding of the effect of elevated temperature and of
547 cementitious matrix nature on properties of TRC. It describes the experimental work developed
548 in order to compare thermal and thermomechanical properties of two types of glass TRCs
549 (3G.AR and 3G.AR.Fire) made with different cementitious matrices (normal mortar and fire
550 mortar respectively) and three identical layers of alkali-resistant glass grids.

551 The first novelty and achievement of this study is that the ultimate stress and the post-cracked
552 composite stiffness of TRC under thermomechanical condition are significantly influenced by
553 the size of particles within the cementitious matrix of TRC. The ultimate stress, when measured
554 as a function of temperature levels, is higher in the normal mortar (3G.AR) than the fire mortar

555 (3G.AR.Fire) because the size of particles within the cementitious matrix is finer for the normal
556 mortar. The ultimate stress of both glass TRC decreases between 25 °C and 120°C, whereas it
557 increases between 120 °C and 300 °C in both cases. For temperature levels above 300°C, the
558 TRC material is strongly damaged by temperature effect, the ultimate stress and the post-
559 cracked composite stiffness of TRC progressively decrease when temperature increases.

560 The second novelty and achievement of this study is that the use of a fire matrix for TRC allows
561 improving the thermal and mechanical stability of TRC that is simultaneously subjected to a
562 tensile pre-load and exposed to increasing elevated temperature. The thermal diffusivity of the
563 fire mortar is weaker than that of the normal mortar which makes the 3G.AR.Fire more
564 thermally stable at a certain stress ratio than the 3G.AR.

565 The third novelty and achievement of this study is that the evolution of thermomechanical
566 behaviour of the two TRCs before 300 ° C has been experimentally justified and analyzed
567 thanks to physical, chemical and thermal characterization. This study highlights that between 25
568 °C and 110 °C, the decrease of the ultimate stress and of the post-cracked composite stiffness of
569 TRC corresponds to dehydration of components of cementitious matrix accompanied by a
570 release of water molecules and creation of micro-cracks. However, between 110 °C and 300 °C
571 with water molecules released, hydration of anhydrous particles of the cementitious matrix of
572 TRC occurs, a gain in the ultimate stress and in the post-cracked composite stiffness of glass
573 TRC consequently manifests.

574 From an application point of view, in thermomechanical conditions at elevated temperatures
575 (fire), it is important to have a stability of the mechanical properties of TRC according to
576 increasing temperature. In order to have a good interaction between the fire cementitious matrix
577 and the textile, it is necessary to develop a finer granulometry for the fire cementitious matrix.
578 In the future, it would be interesting to study a new refractory (fire) cementitious matrix
579 (mortar) with finer aggregates in order to improve “fibers/ refractory matrix” interfaces within
580 this cementitious matrix (mortar). The new refractory (fire) cementitious matrix (mortar) will
581 have better thermal and mechanical properties.

582 7 ACKNOWLEDGMENTS

583 This research was performed with the financial subvention of the European Regional Development Fund
584 (ERDF or FEDER, grant reference: FUI-AAP18-PRORETEX II-Techtera, FEDER 15.008780.01 UCBL)
585 of the European Union and of the Rhône-Alpes-Auvergne region, France for the lot 5 “Characterisation of
586 composite materials” of the PRORETEX II research project. This project is a collaborative research
587 project between four industrial partners (SULITEC - project leader; FOTIA; ER2I; CIMEO) and two
588 academic partners (UCBL/LMC2; ENISE/LTDS). We also would like to thank the team of technicians
589 (Mr. Emmanuel JANIN, Mr. Nobert COTTET) from the Civil Engineering Department at IUT Lyon 1
590 and LMC2, University Lyon 1, for their technical support.

591 8 REFERENCES

- 592 [1] Orłowsky J, Raupach M. Textile reinforced concrete - from research to application. Cement Wapno
593 Beton 2011; 16: 323-330.
- 594 [2] Brameshuber W. Textile Reinforced Concrete. State-of-the-Art Report of RILEM Technical
595 Committee 201-TRC. RILEM Report 2006; 36.
- 596 [3] Florentia A. Kariou, Savvas P. Triantafyllou, Dionysios A. Bournas. The effectiveness of the textile
597 reinforced mortar (TRM) strengthening technique on clay brick masonry arches is investigated .
598 Composites Part B: Engineering 2019 ;173 : 106765.
- 599 [4] Marcari G, Basili M, Vestroni F. Experimental investigation of tuff masonry panels reinforced with
600 surface bonded basalt textile-reinforced mortar. Composites Part B: Engineering 2017; 108: 131–142.
- 601 [5] Benben L, Haibei X, Jiafei J, Xiangxiang D. Tensile behavior of basalt textile grid reinforced
602 Engineering Cementitious Composite. Composites Part B: Engineering 2019 ; 156 : 185-200
- 603 [6] Santis SD, Felice G. Tensile behaviour of mortar-based composites for externally bonded
604 reinforcement systems. Composites Part B: Engineering 2015; 68: 401–413.
- 605 [7] Zoi C. Tetta, Thanasis C. Triantafillou, Dionysios A. Bournas. On the design of shear-strengthened
606 RC members through the use of textile reinforced mortar overlays. Composites Part B: Engineering
607 2018;147 : 178-196.
- 608 [8] Munck M.D., Tysmans T., Wastiels J., Kapsalis P., Vervloet J., El Kadi M.I, Remy O. Fatigue
609 behaviour of textile reinforced cementitious composites and their application in sandwich elements,
610 Applied Sciences (MDPI), 2019, 9(7), 1293
- 611 [9] Kapsalis P., El Kadi M., Vervloet J., De Munck M., Wastiels J., Triantafillou T., Tysmans T.,
612 Thermomechanical behavior of textile reinforced cementitious composites subjected to fire, Applied
613 Sciences (MDPI), 2019, 9, 747.
- 614 [10] S. Xu, L. Shen, J. Wang. The high-temperature resistance performance of TRC thin-plates with
615 different cementitious materials: experimental study, Constr. Build. Mater 115 (2016) 506-519.
- 616 [11] T. Hulin, D.H. Lauridsen, K. Hodicky, J.W. Schmidt, H. Stang. Influence of basalt FRP mesh
617 reinforcement on high-performance concrete thin plates at high temperatures, J. Compos. Constr. 20(1)
618 (2015).
- 619 [12] D. Ehlig, F. Jesse, M. Curbach. High temperature tests on textile reinforced concrete (TRC) strain
620 specimens. In: W. Brameshuber (Eds.), 2nd ICTRC, Textile Reinforced Concrete. Proceeding of the Inter.

621 RILEM Conf. on Material Science (MatSci) v.I (PRO 75), RILEM. Publications SARL, Aachen (2010)
622 141-151.

623 [13] T Büttner, Orlowsky J, Raupach M. Fire resistance tests of textile reinforced concrete under static
624 loading - results and future developments, Proceeding of the 5th Inter. RILEM Workshop on High
625 Performance Fiber Reinforced Cement Composites (HPFRCC5) (2014) 361-370.

626 [14] H.W. Reinhardt, M. Krüger, M. Raupach. Behavior of textile-reinforced concrete in fire. ACI
627 Special Publication 250 (2008) 99-110.

628 [15] Nonnet E, Lequeux N, Boch P. Elastic properties of high alumina cement castables from room
629 temperature to 1600 °C. Journal of the European ceramic society 1999; 19 : 1575–1583.

630 [16] Soro J, Smith A, Gault G. Thermomechanical characteristics of calcium aluminate cement and sand
631 tapes prepared by tape casting. Journal of the European ceramic society 2006; 26, 3799-3807.

632 [17] Sarvaranta L, Mikkola E. Mortars containing wood-based fibres under thermal exposure using cone
633 calorimeter heating. Fire & Materials 1995; 19 (1): 35–41.

634 [18] Sarvaranta L, Mikkola E. Fibre mortar composites in fire conditions. Fire & Materials 1994;18 (1):
635 45–50.

636 [19] Sarvaranta L, Elomaa M, Järvelä E. A study of spalling behaviour of PAN fibre-reinforced concrete
637 by thermal analysis. Fire & Materials 1993; 17 (5): 225–230.

638 [20] Trník A, Scheinherrová L, Medved I, Černý R. Simultaneous DSC and TG analysis of high-
639 performance concrete containing natural zeolite as a supplementary cementitious material. Journal of
640 Thermal Analysis & Calorimetry 2015; 121(1): 67–73. 645

641 [21] Nguyen N.M.T., Yoob D.-Y., Kim J.J., Cementitious material reinforced by carbon nanotube-Nylon
642 66 hybrid nanofibers: Mechanical strength and microstructure analysis. Materials Today Communications
643 23 (2020) 100845

644 [22] Gen Li, Zhang L W. Microstructure and phase transformation of graphene-cement composites under
645 high temperature. Composites Part B: Engineering 2019; 166 : 86-94.

646 [23] Vejmelková E, Koňáková D, Scheinherrová L, Doleželová M, Černý R. High temperature durability
647 of fiber reinforced high alumina cement composites. Constr. and Building Materials 2018 ; 162 :881-891.

648 [24] Kang X., Zhuc X., Liua J., Shu X., Qiand J., Huang Y. Hydration of C3A/gypsum composites in the
649 presence of graphene oxide, Materials Today Communications 23 (2020) 100889

650 [25] Wang G, Zhang C, Zhang B, Li Q, Shui Z. Study on the high temperature behaviour and rehydration
651 characteristics of hardened cement paste. Fire & materials 2015; 39: 741-750.

652 [26] Donnini J, Basalo FDC, Corinaldesi V, Lancioni G, Nanni A. Fabric-reinforced cementitious matrix
653 behavior at high-temperature: experimental and numerical results. Composites Part B: Engineering 2017;
654 108 : 108-121.

655 [27] M.T. Tran, X.H.Vu, E. Ferrier. Mesoscale experimental investigation of thermomechanical
656 behaviour of the carbon textile reinforced refractory concrete under simultaneous mechanical loading and
657 elevated temperature. Construction and Building Materials 217, 2019, 156-171.

658 [28] T.H. Nguyen, X.H. Vu, A. Si Larbi, E. Ferrier. Experimental study of the effect of simultaneous
659 mechanical and high-temperature loadings on the behaviour of textile-reinforced concrete (TRC).
660 Construction & Building Materials 2016 ;125 : 253-270.

661 [29] O. Homoro, X.H.Vu, E. Ferrier. Experimental and analytical study of the thermo-mechanical
662 behaviour of textile-reinforced concrete (TRC) at elevated temperatures: role of discontinuous short glass
663 fibres. *Construction and Building Materials* (190), 2018, 645-663.

664 [30] Tlaji T, Vu XH, Ferrier E, Si Larbi A. Thermomechanical behaviour and residual properties of
665 textile reinforced concrete (TRC) subjected to elevated and high temperature loading: Experimental and
666 comparative study. *Composites Part B : Engineering* 2018 ;144 : 99–110.

667 [31] European standard BS EN 413-2:2005 January 2006 : Masonry cement - Part 2 : test methods; 2005.

668 [32] European standard BS EN 196-1 : Methods of testing cement. Determination of strength; 2005.

669 [33] Green MF, Benichou N, Kodur VKR, Bisby LA. Design guidelines for fire resistance of FRP
670 strengthened concrete structures. Eighth International Conference on FRP in Reinforced Concrete
671 Structures (FRPRCS-8) 2007.

672 [34] Wallenberger FT, Brown SD. High-modulus glass fibers for new transportation and infrastructure
673 composites and new infrared uses. *Composites Science & Technology* 1994; 51, pp 243-263.

674 [35] RILEM Technical Committee 232-TDT (Chair: Wolfgang Brameshuber). Recommendation of
675 RILEM TC 232-TDT: test methods and design of textile reinforced concrete. *Materials and Structures*
676 2016;49(12):4923-49237.

677 [36] Contamine R, Si Larbi A, Hamelin P. Contribution to direct tensile testing of textile reinforced
678 concrete (TRC) composites, *Materials Science & Engineering* 2011; 528: 8589– 8598.

679 [37] Sha W, O'Neill EA, Guo Z. Differential scanning calorimetry study of ordinary Portland cement.
680 *Cement & Concrete Research* 1999, 29 (9), 1487–1489

681 [38] Noumowé A. Effet des hautes températures (20 °C–600 °C) sur le béton, PhD thesis, Institut
682 National des Sciences Appliquées 1995 [in French].

683 [39] Alarcon-Ruiz L, Platret G, Massieu E, Ehrlacher A. The use of thermal analysis in assessing the
684 effect of temperature on a cement paste. *Cement & concrete research* 2005 ; 35(3) :609-613.

685 [40] Michel M. Accélération du ciment au laitier par du ciment sulfo-alumineux. Ph.D thesis, Institut
686 National des Sciences Appliquées de Lyon 2009 [in French].

687 [41] Zhou Q, Glasser F.P. Thermal stability and decomposition mechanisms of ettringite at <120°,
688 *Cement & Concrete Research* 2001; 31 (9), 1333–1339.

689 [42] Khoury G.A. Compressive strength of concrete at high temperatures: A reassessment. *Magazine of*
690 *concrete research* 1992; 44 (161), 291–309.

691 [43] Grattan-Bellew P.E. Microstructural investigation of deteriorated Portland cement concretes.
692 *Construction & Buildings Materials* 1996; 10 (1), 3-16.

693 [44] Nguyen V.A., Vu X.H. Themomechanical behavior at elevated temperature of mortars reinforced by
694 textile. Report of research Master 2, University Lyon 1, 2015.